Available online at www.eccomasproceedia.org
Eccomas Proceedia COMPDYN (2023) 3708-3731

ECCOMAS
Proceedia

COMPDYN 2023
9th ECCOMAS Thematic Conference on
Computational Methods in Structural Dynamics and Earthquake Engineering
M. Papadrakakis, M. Fragiadakis (eds.)
Athens, Greece, 12-14 June 2023

APPLICATION OF THE WAVELET TRANSFORM INVERSE ANALYSIS FOR MODAL IDENTIFICATION AND DAMAGE DETECTION

Pierre Argoul[1,2] and Michalis Fragiadakis[2,3]

[1]LVMT, Ecole des Ponts, Université Gustave Eiffel
77454 Marne la Vallée, France
e-mail: pierre.argoul@enpc.fr

[2]Gustave Eiffel University, MAST-EMGCU
F-77454 Marne-la-Vallee, France
e-mail: pierre.argoul@univ-eiffel.fr

[3]National Technical University of Athens
Iroon Polytechneiou 15780, Zografou Campus, Athens, Greece
e-mail: mfrag@mail.ntua.gr

Abstract. *The paper discusses the application of the Continuous Wavelet Transform method for modal identification and structural damage detection. The wavelet transform method can be applied for understanding the responses of different structures under various loading conditions, i.e. signals impact embedded in noise, or strong seismic loading. The method provides the representation in the time-frequency plane of the processed signal thus allowing to estimate the modal characteristics or to that of the structural defects (localization in time and severity of the damage). The paper summarizes the important aspects of the method and proposes a novel formulation for structural damage assessment. Two example applications are presented, a four degree-of-freedom linear system that freely oscillates and a single-degree-of-freedom oscillator initially subjected to harmonic loading and subsequently left to freely oscillate. The examples show that the CWT method can be used to obtain valuable information for structural damage assessment.*

Keywords: wavelet transform, modal identification, damage detection, building vibrations

doi: 10.7712/120123.10674.22675

1 INTRODUCTION

The Wavelet Transform (WT) method appeared in mathematics more than a century ago, starting with Haar who discovered in 1909 an orthonormal basis consisting of step functions. The Haar basis construction is a precursor of what is known as the multiresolution analysis [1] which refers to the expansion of a signal into components that can reproduce the original signal when added together. The principle of multiresolution spaces is to decompose a signal of finite energy $\mathcal{L}^2(\mathbf{R})$ to two complementary spaces: (i) a space of approximation; and (ii) a detail space that contains the approximation error. Multi-resolution analysis can be seen as a way to zoom into, or out, of the signal without losing information. From the beginning of 1980s, under the impetus of several French researchers, especially Grossmann and Morlet [2], wavelet research in mathematics has grown steadily with significant contributions from many authors. Figure 1 provides a quick overview of the history of the WT method. Since then, the WT has been used in many areas of science and engineering. Here, for example, is a recent reference published by A. Guillet and his co-workers, applied to physiological signals. In [14], the authors introduced time-log-frequency ratio distributions based on WT with analytic mother wavelets (the Grossmann wavelet belonging to the Morse wavelets family cf. [19]) that they applied to voice records. Two main trends exist in how the WT is computed and used: the Continuous Wavelet Transform (CWT) and the Discrete Wavelet Transform (DWT) method [3]. Our work will focus on the former.

Figure 1: Short History of Wavelet Transform (WT).

An interesting analogy between time-frequency (TF) analysis and modern music notation is shown in Figure 2. Modern music notation gives an illustration of the time-frequency representation of the time-frequency representation where the vertical position of the note-head within the staff indicates its pitch which can be modified by accidentals, associated with a frequency (the frequency of A3, for example, is set at 440 Hz). The time duration (note length, or note value) is indicated by the form of the note-head or with the addition of a note-stem plus beams or flags (cf. 2).

Among the large number of books on wavelet transform [4, 6, 3], few are dedicated to applications to civil engineering structures. The book by Chatterjee [7] describes several applications of wavelets to civil engineering problems and shows their importance, for example, in the analysis of non-stationarities in seismic ground motions, in the study of bridge vibrations caused by vehicle passage, or in the identification of structural damage. Furthermore, damaging events often result in short-time, non-stationary vibration characteristics that are difficult to analyse using classical modal approaches. Methods based on time-frequency representations, such as wavelet transform methods, are better suited to analysing signals generated by time-varying systems than those using the Fourier transform that are better suited to signals generated by time-invariant systems. This makes these time-frequency based methods a very interesting tool for structural damage detection.

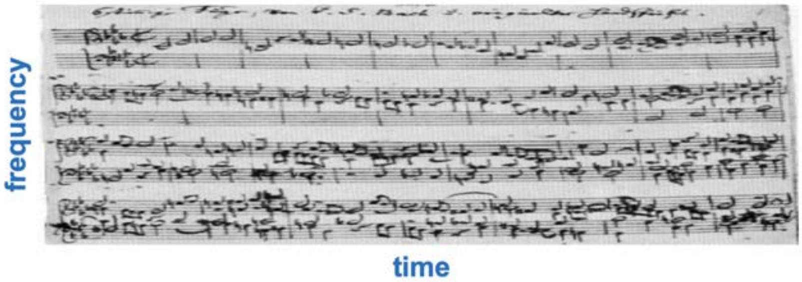

Figure 2: Writing of a musical piece: a famous illustration of time-frequency representation.

2 THE CONTINUOUS WAVELET TRANSFORM METHOD

The basic idea of the Continuous Wavelet Transform (CWT) method is to use a function $\psi(t) \in L^1(\mathbb{R}) \cap L^2(\mathbb{R})$ called the "mother wavelet"[1], which can generate an infinite continuous basis of functions, by varying parameters a and b:

$$\psi_{a,b}(t) = (1/a)\psi[(t-b)/a], \tag{1}$$

where a is a scale parameter and b a temporal localization parameter.

There is a clear relationship between scale a and frequency f. More specifically, a low value of a results in a compressed wavelet, allowing to capture the details in the processed signal that change rapidly, thus resulting in a high frequency content. On the other hand, a large scale of a results in a stretched wavelet, which captures slowly changing coarse features in the processed signal, resulting in a high frequency content. Thus $1\ /\ a$ can be assimilated to a frequency parameter f. There are several possible approaches that relate the scale a to the inverse of the frequency, typically denoted: $a = f_\psi^*/f$. In the references [8, 10], f_ψ^* is chosen to be equal to the peak frequency f_ψ^0, where $f_\psi^0 = \arg\max(|\widehat{\psi}|)$ and $\widehat{\psi}$ is the Fourier transform of the mother wavelet. Two other meaningful frequencies, classically found in literature, are the energy frequency: $\tilde{f}_\psi$[2]. and the time-varying instantaneous frequency of the wavelet at its

[1] A function $\psi(t) \in L^1(\mathbb{R}) \cap L^2(\mathbb{R})$ can be admissible to a mother wavelet if it satisfies the admissibility condition : $C_\psi = \int_{-\infty}^{+\infty} \frac{|\widehat{\psi}(f)|^2}{|f|} df < \infty$ where $\widehat{\psi}(f) = \int_{-\infty}^{+\infty} \psi(t) e^{-2i\pi f t} dt$ is the Fourier transform of $\psi(t)$, which implies that $\int_{-\infty}^{+\infty} \psi(t) dt = 0$. cf. [4].

[2] $\tilde{f}_\psi = \frac{\int_{-\infty}^{+\infty} f \left|\widehat{\psi}(f)\right|^2 df}{\int_{-\infty}^{+\infty} |\widehat{\psi}(f)|^2 df}$.

time center $\breve{f}_\psi(0)$[3] (cf. [17]). These three definitions of f_ψ^* allow us to define three different mappings between scale and frequency. The first will correctly give the frequency of a pure cosine on the scale a at which its CWT reaches a maximum . The second will correctly give the frequency of a pure cosine from the energy mean scale of the CWT $\widetilde{a_\psi}(b)$ [4]. The last sets the frequency to match the phase of the CWT at the location of an infinitesimally small pulse.

The first will correctly give the frequency of a pure harmonic signal from the scale a at which its transform obtains a maximum, the second will correctly give the frequency of a pure harmonic signal from the energy-mean scale of the transform, and the third fixes the frequency to be the same as the phase progression of the transform at the location of an infinitesimally narrow impulse. To better highlight the importance of the choice of f_ψ^0, consider the example of the CWT of a cosine $u(t) = A_1 \cos(2\pi f_1 t + \theta_1)$. The CWT can be written as: $T_\psi[u](a,b) = \frac{1}{2} A_1 \widehat{\psi}(af_1)\, e^{i\theta_1}$ and its modulus $|T_\psi[u](a,b)| = \frac{1}{2} A_1 |\widehat{\psi}(af_1)|$ is maximal when $|\widehat{\psi}(af_1)|$ is maximal, so that $af_1 = f_\psi^0$ and $|T_\psi[u](a,b)| = A_1$. In addition, the energy mean scale of the CWT $\widetilde{a_\psi}(b)$ in the case of a pure cosine is equal to: $\widetilde{a_\psi}(b) = \tilde{f}_\psi \,/\, f_1$ [5].

Using a mother wavelet ψ, the CWT method is then used to decompose a function $u(t)$ into the time-frequency domain as follows:

$$T_\psi[u](a,b) = \frac{1}{a} \int_{-\infty}^{+\infty} u(t) \overline{\psi}\left(\frac{t-b}{a}\right) dt, \tag{2}$$

where $\overline{\psi}$ is the conjugate of ψ.

Regarding the regularizing term $1/a$ in the definition of Eq. 2. This term is appropriate when the magnitude of the modulus wavelet transform is wished to reflect the amplitude of the analysed signal $u(t)$. It is generally more useful to describe time-localized signals by their amplitude; hence, Eq. 2 uses the $1/a$ normalization which is known as the L_1 norm, it is used in Carmona *et al.* [4], preferred by Argoul [12, 13] or Lilly[15]. Instead, the factor $1/\sqrt{a}$ can guarantee that the wavelet maintains constant energy. This is known as the L_2 norm of T_ψ and is more appropriate when one wishes that the modulus-squared wavelet transform reflects the energy of the analyzed signal.

The definition of CWT of Eq. 2 can be rewritten in the frequency domain:

$$T_\psi[u](a,b) = \int_{-\infty}^{+\infty} \widehat{u}(f) \widehat{\psi}\,(af)\, e^{2i\pi fb} df, \tag{3}$$

where $\widehat{u}(f) = \int_{-\infty}^{+\infty} u(t) e^{-2i\pi ft} dt$ is the Fourier transform of $u(t)$ and $\widehat{\psi}$ is the mother wavelet in the frequency domain. Eq. 3 allows for an easy numerical computation by means of the fast Fourier transform algorithm.

2.1 Selection of mother wavelet

Apart from the widely-used Morlet wavelet, which is only approximately analytic, various analytic wavelets have been proposed, including the Cauchy-Paul, the derivative of the Gaussian wavelet, the lognormal or log Gabor, the Shannon, the Bessel, among others. Olhede and

[3] $\breve{f}_\psi(t) = \frac{1}{2\pi} \frac{d}{dt} \Im\{\ln \psi(t)\} = \frac{1}{2\pi} \frac{d}{dt} \left(arg\{\psi(t)\}\right).$

[4] $\widetilde{a_\psi}(b) = \frac{\int_{-\infty}^{+\infty} a\,|T_\psi[u](a,b)|^2 da}{\int_{-\infty}^{+\infty} |T_\psi[u](a,b)|^2 da}.$

[5] $\widetilde{a_\psi}(b) = \frac{\int_{-\infty}^{+\infty} a\,|T_\psi[u](a,b)|^2 da}{\int_{-\infty}^{+\infty} |T_\psi[u](a,b)|^2 da} = \frac{\frac{1}{4} A_1^2 \int_0^{+\infty} a \left|\widehat{\psi}(af_1)\right|^2 da}{\frac{1}{4} A_1^2 \int_0^{+\infty} \left|\widehat{\psi}(af_1)\right|^2 da} = \frac{1}{f_1} \frac{\int_0^{+\infty} f \left|\widehat{\psi}(f)\right|^2 df}{\int_0^{+\infty} \left|\widehat{\psi}(f)\right|^2 df} = \frac{\tilde{f}_\psi}{f_1}.$

Walden [16] and Lilly and Olhede [17] have showed that all known analytic wavelets can be grouped together in a much larger family, first introduced by Daubechies and Paul [18], whose properties were studied in detail [19]. This broad "superfamily" of wavelets is known as the generalized Morse wavelets. Within that family, one can objectively say which wavelet choice is the "best" for the problem at hand. The generalized Morse wavelets $\psi_{\beta,\gamma}$ depend on two parameters β and γ which control its form and the general expression is:

$$\widehat{\psi}_{\beta,\gamma}(f) = c_{\beta,\gamma} f^{\beta} e^{-(2\pi f)^{\gamma}} H(f) \tag{4}$$

where $c_{\beta,\gamma}$ is a normalization constant and $H(f)$ is the unit step function.

The Cauchy-Paul mother wavelet $\psi_n(t)$ has been preferred in our work, among the broad family of generalised Morse wavelets. This is a complex single parameter mother wavelet where n is an integer that controls the shape of the wavelet. With respect to Eq. 4, the Cauchy-Paul wavelet belongs to the Morse family when $\beta = n$ and $\gamma = 1$, while the definition with respect to parameter n, becomes:

$$\widehat{\psi}_n(f) = c_n\, f^n e^{-2\pi f} H(f) \tag{5}$$

where c_n is a normalization constant. An asymmetry in the frequency domain of the Cauchy-Paul wavelet leads to distinct values for the frequencies previously introduced in order to define the scale parameter $a = f_{\psi}^{*}/f$, i.e.:

$$f_{\psi_n}^{0} = \frac{n}{2\pi}, \quad \tilde{f}_{\psi} = \frac{n+\frac{1}{2}}{2\pi}, \quad \breve{f}_{\psi_n} = \frac{n+1}{2\pi}, \tag{6}$$

There are several ways to define the c_n parameter. In older papers [11, 12, 13] we preferred the L^{∞} norm in the time domain: $\|\psi_n\|_{\infty} = 1$. In this paper we have chosen the following norm: $\|\widehat{\psi}_n\|_{\infty} = \max|\widehat{\psi}_n(f)| = 2$, which leads to $c_n = 2(2\pi e/n)^n$. The peak frequency is: $f_{\psi}^{0} = n/2\pi$, for which the maximum value is: $\widehat{\psi}_n(f_{\psi}^{0}) = 2$. This is the same choice as in Lilly [15], as it gives a direct equality between $|T_{\psi}[u](t, a(t))|$ and the amplitude of u.

There are several reasons for choosing an analytic mother wavelet, and the Cauchy-Paul wavelet in particular. The first is that an analytic mother wavelet which is a complex function whose spectrum contains only positive frequencies, leading to: $\widehat{\psi}_n(f) = 0\ \forall\ f < 0$. As an analytic mother wavelet only responds to non-negative frequencies in the signal being analysed, it produces a transform whose modulus is less oscillatory than in the case of a real mother wavelet. This property is a real advantage for detecting and tracking the instantaneous frequencies contained in the signal. Eq. 3 is simplified as follows:

$$T_{\psi}[u](a,b) = \int_{0}^{+\infty} \widehat{u}(f)\widehat{\psi}\,(af)\, e^{2i\pi fb} df. \tag{7}$$

The second reason concerns the phase retrieval problem which is the reconstruction of a function from its scalogram, that is, from the modulus of its wavelet transform. Mallat and Waldspurger [20] mathematically proved that the reconstruction of the analyzed function from the modulus of its Cauchy-Paul wavelet transform is unique up to a global phase. They also showed that the reconstruction operator is continuous but non uniformly continuous. The authors specify that the proofs are special to Cauchy-Paul wavelets and cannot be extended to generic wavelets because they make intensive use of the link between Cauchy wavelets and holomorphic functions.

2.2 Resolution in the time-frequency domain

For the successful CWT decomposition, it is essential to control the *time-frequency resolution* of the signal wavelet transform. This is necessary in order to correctly interpret the CWT plot and also to take into account *edge effects* [13]. Referring to the conventional frequency analysis of constant-Q filters, Le and Argoul [13] introduced a parameter Q_m called "quality factor" that can be used in order to control the time-frequency resolution of the CWT. Introducing the duration Δt and the frequency bandwidth Δf of the wavelet transform and its relationship with the the duration Δt_ψ and the frequency bandwidth Δf_ψ of the mother wavelet are as follows:

$$\Delta t \;=\; a\,\Delta t_\psi \qquad\qquad \Delta f \;=\; \frac{\Delta f_\psi}{a}, \tag{8}$$

where Δt_ψ and Δf_ψ are stated in terms of root mean squares for L_2 norm which are equivalent to standard deviations in statistics:

$$\begin{aligned}
\Delta t_\psi &= \frac{1}{\|\psi\|_2^2}\int_{-\infty}^{+\infty}\left(t-t_\psi\right)^2\,|\psi(t)|\,dt\\
\Delta f_\psi &= \frac{1}{\|\widehat{\psi}\|_2^2}\int_{-\infty}^{+\infty}\left(f-f_\psi\right)^2\,|\widehat{\psi}(f)|^2\,df,
\end{aligned} \tag{9}$$

where t_ψ and f_ψ are the centre of ψ and $\widehat{\psi}$, respectively:

$$t_\psi \;=\; \frac{1}{\|\psi\|_2^2}\int_{-\infty}^{+\infty} t\,|\psi(t)|^2\,dt \qquad\qquad f_\psi \;=\; \frac{1}{\|\widehat{\psi}\|_2^2}\int_{-\infty}^{+\infty} f\,|\widehat{\psi}(f)|^2\,df. \tag{10}$$

It is noteworthy to introduce the CWT uncertainty μ, equal to the mother wavelet uncertainty μ_ψ:

$$\mu \;=\; \Delta t\,\Delta f \;=\; \Delta t_\psi\,\Delta f_\psi \;=\; \mu_\psi \tag{11}$$

Using the relationship between scale and frequency previously discussed $(a \;=\; f_\psi^*/f)$, Eq. 8 becomes:

$$\Delta t \;=\; \frac{f_\psi^*\,\Delta t_\psi}{f} \propto \frac{1}{f} \qquad\qquad \Delta f \;=\; \frac{\Delta f_\psi}{f_\psi^*}\,f \propto f, \tag{12}$$

This Q_m factor introduced in [13] is defined as the ratio of the mean value $\tilde{f}$ (for L_2 norm) previously defined over two times its standard deviation Δf of the wavelet transform, i.e.:

$$Q_m = \frac{\tilde{f}}{2\Delta f} = \frac{\frac{\tilde{f}_\psi}{a}}{2\frac{\Delta f_\psi}{a}} = \frac{\tilde{f}_\psi}{2\Delta f_\psi}. \tag{13}$$

Notice from Eq. 13 that the resolution parameter Q_m is independent of the frequency parameter a. From the formulae above, it is easy to see that:

$$\Delta t \;=\; 2\,Q_m\,\mu_\psi\frac{f_\psi^*}{\tilde{f}_\psi}\,\frac{1}{f} \qquad\qquad \Delta f \;=\; \frac{1}{2\,Q_m}\,\frac{\tilde{f}_\psi}{f_\psi^*}\,f. \tag{14}$$

where the ratio $\frac{\tilde{f}_\psi}{f_\psi^*}$ is close to 1 and equal to 1 if $f_\psi^* \;=\; \tilde{f}_\psi$; for example for Cauchy wavelet it depends on the value of n (Eq. 6).

Thus, a small Q_m value increases the resolution in the time axis (Δt small), while a large value increases the frequency resolution (Δf small).

Properly adjusting the Q_m parameter is particularly important in the case of two close Eigenmodes which allows to separate them. In reference [13], it was shown that the value of Q_m can be chosen within the limits below:

$$Q_m^{(min)} = c_f \frac{f_j}{2\,Df_j} \leq Q_m \leq Q_m^{(max)} = \frac{\pi L f_j}{c_t}, \tag{15}$$

where L is the length of the signal, c_t, c_f are constants that are used to identify edge effects in the time and the frequency domain, respectively, f_j is the Eigenfrequency of interest and Df_j is its distance from the closest Eigenfrequency. Note that typically c_t and c_f receive values between 3 and 5. Another important point of interest is that when the Q_m value increases, the edge effects become more significant, thus the useful time interval for modal identification is reduced but the decoupling of the modes is more effective.

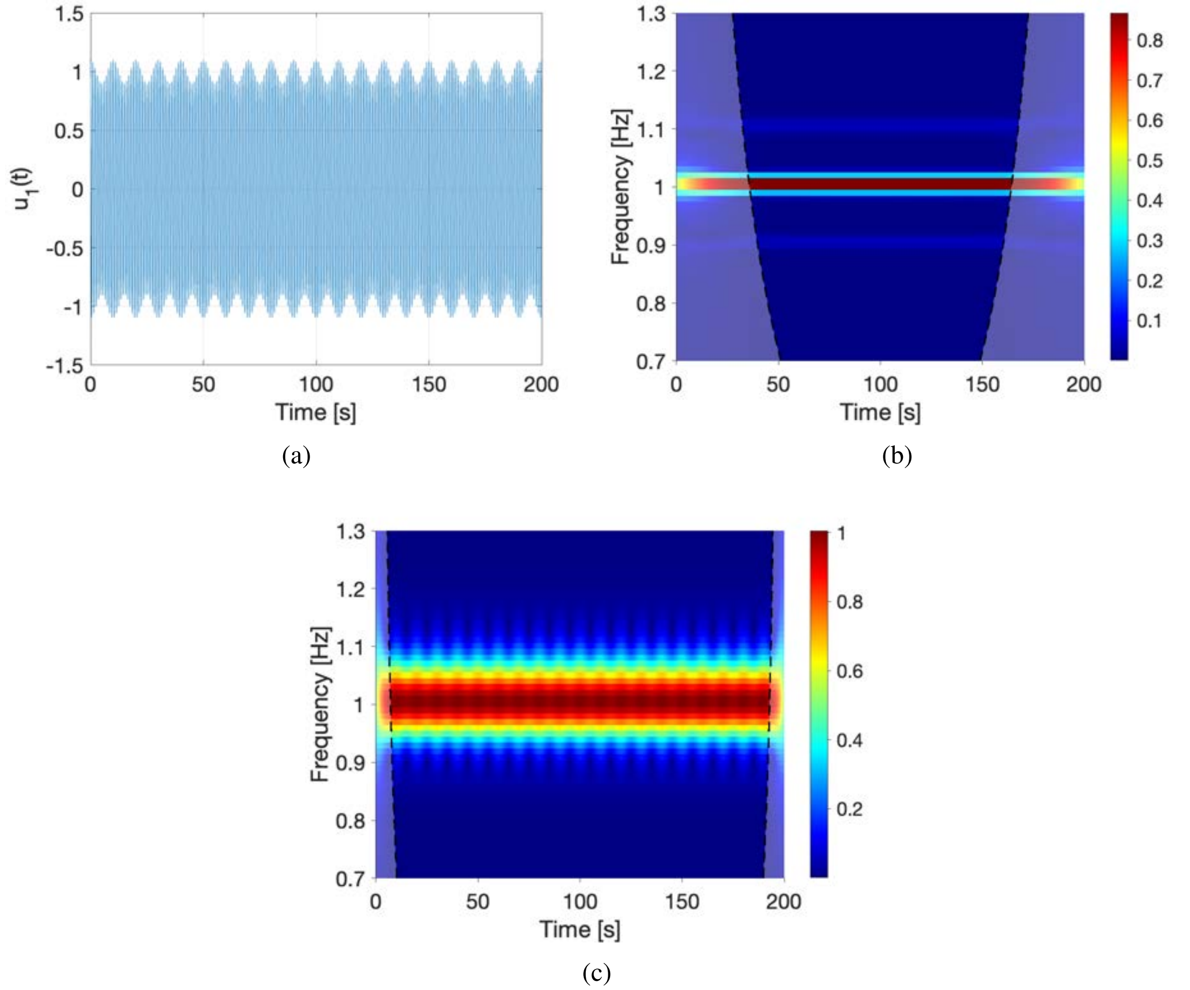

Figure 3: Wavelet analysis on a amplitude-modulated signal $u_1(t) = A(t)\cos(2\pi t)$ with $A(t) = 1 + 0.2\cos(2\pi t/10)$: (a) the signal $u_1(t)$ in the time domain, (b) scalogram computed with $Q_m = 75$ and (c) scalogram computed with $Q_m = 15$.

The importance of the resolution parameter can be understood from the two examples of Figures 3 and 4. The figures present two examples of signals, with their time-frequency scalogram plots.

The first example concerns the amplitude modulated signal $u_1(t) = A(t)\cos(2\pi t)$, where $A(t) = 1 + 0.2\cos(2\pi t/10)$ (Figure 3a). The expression for $u_1(t)$ can be misleading. By developing the equation using trigonometric formulae, it can be shown that $u_1(t)$ is the sum of three cosines: $u_1(t) = \cos(2\pi t) + 0.1\ \cos(\frac{11}{10}\,2\pi t) + 0.1\ \cos(\frac{9}{10}\,2\pi t)$ which can be identified in the scalogram plot of Figure 3b) as three horizontal ridges. Due to the amplitude dominance of the first term at 1Hz, the other two frequencies at $9/10$ and $11/10$Hz cannot be seen unless the quality factor Q_m is chosen "correctly". According to Eq. 15, the bounds are: $Q_m^{(min)} = 25$ and $Q_m^{(max)} = 125.6$ respectively, with $c_t = c_f = 5$, $f_j = 1Hz$, $\Delta f = 1\ /\ 10$ Hz and $L = 200s$. If we had chosen a quality factor lower than $Q_m^{(min)} = 25$, giving precedence to time resolution over frequency resolution, the scalogram plot would have shown oscillations at the edges, as shown in Figure 3c.

The second example (Figure 4) is that of an acoustic signal $u_2(t)$ measured when the passage of a semi-trailer on a joint of pavement in very good condition on a motorway bridge and plotted in Fig. 4a). The frequency content of this signal is mainly between 0 Hz and 2500 Hz (see. Fig. 4b)). Zooming in on the amplitude spectral density of $u_2(t)$, which is the square root of its classical Pseudo Spectral Density (PSD) over this frequency range, we see three main peaks around the frequencies $250, 600$ and 900Hz. Table 1, shows the limits of the Q_m factor: $Q_m^{(min)}$ and $Q_m^{(max)}$, for the three frequency values obtained using Eq. (15). Two scalograms of this signal are then plotted for two different values of the quality factor in Figures 4c) and 4d): $Q_m = Q_m^{(min)} = 2$ and $Q_m = Q_m^{(max)} = 125$, respectively, corresponding to the limits: $Q_m^{(min)} = 2$ and $Q_m^{(max)} = 125$ for the relevant frequency: $f_j = 250Hz$ given in Table 1.

A comparison of these two scalograms provides an obvious interpretation. The lower the value of Q_m, the more visible the time effect is, with the vertical lines corresponding to the times that the 5 axles of the semi-trailer passed over the pavement joint.

Table 1: Values of the limits of the quality factor $Q_m^{(min)}$ and $Q_m^{(max)}$ from Eq. (15) corresponding to the three frequency peaks in the FT of the signal generated by the passage of a semi-trailer over the joint.

Relevant frequency f_j (Hz)	$Q_m^{(min)}$	$Q_m^{(max)}$
250	2	125
600	5	301
900	7.5	452

Another point of interest, also related to Q_m is the *edge-effect* problem. The problem is attributed to the finite length of the signal, the discretization of the measured data record and to the nature of the CWT. Edge effects cannot be removed and there will always be a domain in the time-frequency plane that should be neglected due to this problem. Edge effects are seen with dashed lines in Figs. 3 and 4; the effect of the quality parameter Q_m on edge effects is evident, i.e high frequency resolution increases the area that is affected.

In reference [14], based on a study on simulated digital signals, the authors concluded that the choice of Q_m is a compromise between two objectives, (i) to discriminate close frequencies (in which case larger values of Q_m are preferred), (ii) to adopt a correct temporal resolution

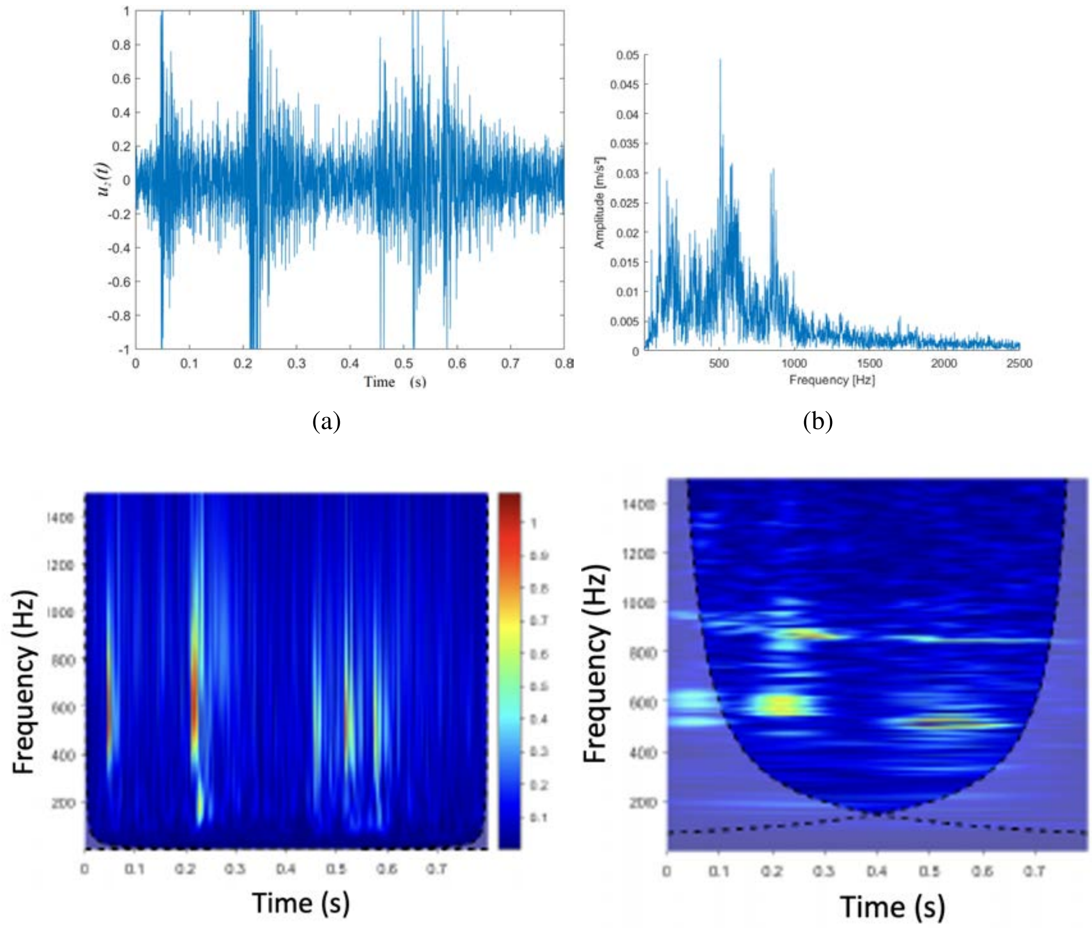

(a) (b)

(c) (d)

Figure 4: Acoustic response $u_2(t)$ of a joint of pavement on a motorway bridge measured when a semi-trailer passes by: (a) time response, the amplitude is normalised between $[-1, 1]$, note that on this recording, the passage of a lorry saturates the microphone, (b) amplitude spectral density of $u_2(t)$ over the range [0, 2500]Hz, (c) Scalogram of $u_2(t)$ computed with $Q_m = Q_m^{(min)} = 2$ for $f_j = 250Hz$ and (d) Scalogram of $u_2(t)$ computed with $Q_m = Q_m^{(max)} = 125$ for $f_j = 250Hz$.

for the detection of abrupt frequency changes (in which case smaller values of Q_m are more effective).

In conclusion, the computation of CWT of Eq. 7 can be performed for $f = f_\psi^0 / a = n / (2\pi a)$ within a chosen frequency band and with an adapted time-frequency resolution Q_m. This remark led Rouby *et al.* [21] to introduce an adapted CWT: $T_\psi[u](f_\psi^0 / f, b)$ with a time-frequency resolution varying for each frequency, leading to a uniform resolution in the whole time-frequency plane.

3 ASYMPTOTIC SIGNALS - RIDGE DEFINITION AND EXTRACTION

3.1 One component signal

Several authors [4, 5, 22, 23] have worked on the use of CWT for so-called asymptotic signals. The typical example is the chirp model [4, 5] which is a pseudo-periodic signal modulated in frequency around a carrier frequency and also modulated in amplitude by an envelope whose variations are slow compared with the oscillations of the phase [23]. The CWT results obtained in the context of asymptotic signals are very useful in particular for modal analysis [13]. The first step is to uniquely associate to any real signal $u(t)$ a canonical amplitude $A^{(u)}(t)$ assumed to be positive and a phase $\theta^{(u)}(t)$ assumed to be increasing, and satisfying: $u(t) = A^{(u)}(t)\,\cos(\theta^{(u)}(t))$. $A^{(u)}(t)$ and $\theta^{(u)}(t)$ can be determined with the aid of the Hilbert transform $\mathcal{H}[u]$ which is defined in the Fourier domain as: $\widehat{\mathcal{H}[u]}(f) = -isgn(f)\,\widehat{u}(f)$ and allows the definition of the analytical signal $Z_u(t)$ associated to $u(t)$ such as:

$$Z_u(t) = u(t) + i\mathcal{H}[u](t) = A^{(u)}(t)\,e^{i\,\theta^{(u)}(t)} \tag{16}$$

Several authors have showed that the CWT of such an asymptotic signal will tend to "concentrate" in the neighborhood of a curve $a_1(t)$ called "ridge" that consists of an aggregation of points called ridge points. Two different definitions of the ridge points are commonly used; they are obtained either from the CWT modulus of the signal or from its phase, and are called *amplitude ridge points* and *phase ridge points*, respectively [24].

In the time-scale map, a ridge can be defined (see reference [23]) from both its canonical phase $\theta^{(u)}$ by:

$$a_1(t) = \frac{2\pi\, f_\psi^*}{\dot{\theta}^{(u)}(t)}, \tag{17}$$

where f_ψ^* appears in the chosen mapping between scale and frequency previously detailed.

The restriction of the CWT to the ridge $a_1(b)$, is called the "skeleton" of the wavelet transform, reproduces the signal itself (or more precisely that of its associated analytical signal $Z_u(b)$) and it behaves like the product of $Z_u(b)$ by a multiplicative factor entirely characterised by the mother wavelet and the ridge $a_1(b)$:

$$T_\psi[u](a_1(b), b) \;=\; \frac{1}{2}\,\overline{\widehat{\psi}}\left(a_1(b)\dot{\theta}^{(u)}(b)\right) Z_u(b) = \frac{1}{2}\,\overline{\widehat{\psi}}\left(2\pi\, f_\psi^*\right) Z_u(b). \tag{18}$$

The process of estimating the ridge from the absolute value and/or the phase information of the CWT of the signal is called "ridge extraction". Different techniques for extracting ridges exist [4] and can be classified into two categories: the "differential" and the "global" methods [13].

Differential methods rely on local properties of the CWT of the signal $u(t)$, verified theoretically on the ridge curve; they are based on the partial differential equations of the CWT. The differential method used here is based on the modulus of $T_\psi[u](a, b)$, which is maximum at b in the vicinity of the ridge, and therefore verifies a cancellation of its partial derivative at a. This definition is given in [24] and its implementation has the advantage that it is particularly simple and stable since it is a simple search for maxima.

The global methods, introduced in reference [25] are based on the search for curves that maximize the energy of the CWT while maintaining a certain regularity of the solution. When the considered frequency and amplitude modulated signal is embedded in noise and near the ridges, the contribution of the signal is much larger than that of the noise, while the wavelet transform of the noise spreads in the whole time-frequency plane. Several algorithms for global ridge extraction are detailed in the book by Carmona *et al.* [4] and are discussed with reference to their robustness to noise.

Once the ridge extraction method has been chosen and the ridge has been determined, the analytical signal $Z_u(b)$ can be obtained. Its real and imaginary parts give the signal and its Hilbert transform, respectively. The final goal of ridge extraction is to get an estimate of $\dot{\theta}_u(t)$ from Eq. 17 and then of $Z_u(b)$ feeding it back into Eq. 18.

3.2 Multicomponent signals

The analytical expression of the structural responses of linear systems is well-known, even in the case of non-proportionally damped systems [26]. The aim of this section is to characterise the behaviour of structures from multi-channel dynamic signals obtained from measurements made by a set of N sensors, typically accelerometers. The set of displacement measurements at these sensor points is grouped into the vector: $\mathbf{u} = [u_1, u_2, \cdots, u_N]^T$. Note that this notation is generic and can also be used when the signal is an acceleration. The modal decomposition expresses the state equation as a linear combination of the various modes of the system Thanks to modal decomposition for linear systems, each signal can be expanded as a linear combination of the different modes of the system, e.g. M components, each corresponding to a different eigenmode of the structure [26]. The CWT of each component of $\mathbf{u}$ is also grouped in the vector $\boldsymbol{T}_\psi[\mathbf{u}]$, as follows:

$$\boldsymbol{T}_\psi[\mathbf{u}](a,t) = \left[T_\psi[u_1](a,t), T_\psi[u_2](a,t), \ldots, T_\psi[u_N](a,t)\right]^T \tag{19}$$

Therefore, the displacement $u_k(t)$, taking into account the M modes, can be obtained as:

$$u_k(t) = \Re \sum_{l=1}^{M} \left\{ A_l^{(u_k)}(t)\, e^{i\,\theta_l^{(u_k)}(t)}\, \Phi_k^{(l)} \right\}, \tag{20}$$

where $A_l^{(u_k)}(t)\, e^{i\,\theta_l^{(u_k)}(t)}$ is the analytical modal participation factor of the l-th complex mode $\boldsymbol{\Phi}^{(l)}$ ($\Phi_k^{(l)}$ being its k-th component) to the structural response $\boldsymbol{u_k}(t)$, while its real parts $A_l^{(u_k)}(t)\, \cos\left(\theta_l^{(u_k)}(t)\right)$ are assumed to be asymptotic. The vector $\boldsymbol{\Phi}^{(l)}$ is the complex l-th mode, which we have chosen to normalise as follows $\left(\boldsymbol{\Phi}^{(l)}\right)^t\, \boldsymbol{\Phi}^{(l)} = 1$, based on the generalisation of a criterion usually used for real modal deformations: $\left(\boldsymbol{\phi}^{(l)}\right)^t\, \boldsymbol{\phi}^{(l)} = \|\boldsymbol{\phi}^{(l)}\|^2 = 1$ (cf. Carpine [10]). In the case of free responses, the dynamic signals contain the vibrations of each mode of the structure, associated with an exponentially damped sinusoidal component. Thus, Eq. (20) becomes:

$$u_k(t) = \Re \sum_{l=1}^{M} \left\{ A_l^{(u_k)}(t)\, e^{i\,\theta_l^{(u_k)}(t)}\, \Phi_k^{(l)} \right\} = \Re \sum_{l=1}^{M} \left\{ Z_l^{(u_k)} e^{i\,\lambda_l t} \Phi_k^{(l)} \right\}, \tag{21}$$

where $Z_l^{(u_k)}$ is a complex constant and λ_l is the l-th pole: $\lambda_l = 2\pi\, i\, f_l\, \sqrt{1-\xi_l^2} - \xi_l\, 2\pi\, f_l$ and f_l, ξ_l are the Eigenfrequency and the modal damping ratio associated with mode l, respectively.

Thanks to the above form, which is a sum of asymptotic amplitude and frequency modulated components, in the case of a single asymptotic amplitude and frequency modulated signal, the absolute value of its CWT tends to concentrate near the “ridges” of the transform [4]. In the time-frequency plane, this corresponds to a well-defined region, but most importantly, the wavelet transform acts as a “regularizing” filter that concentrates along the ridges the information that is carried within the signal and hence allows to characterize the instantaneous frequencies. Based on the discussion above, the linearity of the CWT and a good choice of the mother wavelet ψ can allow to separate these different components and extract the ridge for each of them. There are several approaches for detecting multiple ridges, the final choice depends on their interaction, or their independence. When these ridges do not interact and are located at distinct regions of the time-frequency plane, a frequently encountered case in the analysis of dynamic signals for which each instantaneous frequency remains in the vicinity of a horizontal straight line, the methods previously mentioned can be implemented as in [13, 27].

As previously discussed, the ridges can then be deduced using the expression:

$$a_l^{(k)}(t) = \frac{2\pi f_\psi^*}{\dot{\theta}_l^{(u_k)}(t)}. \tag{22}$$

Let us thus study the case of a system with two close Eigenfrequencies, f_j and f_k. The possibility of extracting the ridges of two close Eigenfrequencies, is guaranteed if the following condition is satisfied:

$$\xi_j \le \frac{\sqrt{2}}{c_f} \frac{|f_j - f_k|}{f_j}, \tag{23}$$

where c_f is a constant related to edge effects [28], ξ_j is the modal damping ratio of the j-th mode and the j and k indexes correspond to two neighboring modes j and k, respectively. If the condition of Eq. 23 is not met, the extraction of accurate ridges is not guaranteed and may even not be possible since the modes are too close and they cannot be separated when they are heavily damped. This tells us that two close modes cannot be well separated from each other if they are damped too much. Figure 5 plots the ξ_j values as function of f_j and $\Delta f = |f_j - f_k|$ for $c_f = 3$. If the condition of Eq. 23 is met, the extraction of accurate ridges is guaranteed, provided that the quality factor Q_m, as already discussed in Eq. 13 and Section 2.1.

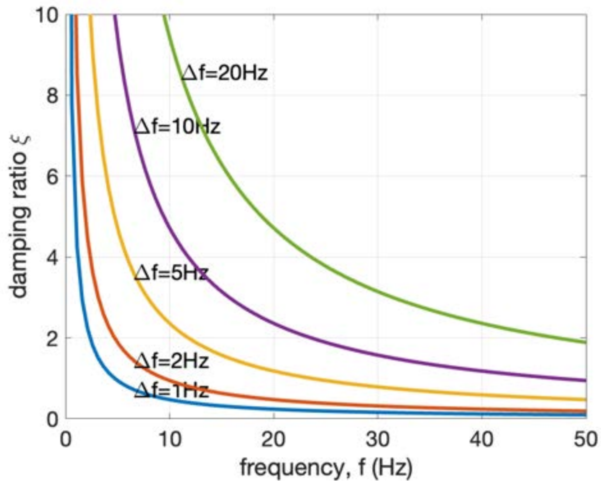

Figure 5: Relationship between damping ration and frequency for ridge identification according to Eq. 23 ($c_f = 3$).

As already discussed, at each measurement point u_k, $k \in [1, N]$, a set of ridges $a_k^{(l)}(t)$ can be extracted from the time-frequency plot, for the l-th mode excited by the shock, where $l = 1, \dots, M$. For the extraction of ridges, differential methods based on a local analysis of the extrema of the CWT modulus are here preferred. Thus the ridges, or the instantaneous frequencies $a_l^{(k)}(t)$, are extracted by the computation of local maxima of $\left|T_\psi[u_k](a,t)\right|$ as function of time t and for the l-th mode excited by the shock:

$$a_l^{(k)}(t) = arg_a max \Big| T_\psi[u_k](a,t) \Big|. \tag{24}$$

So, for a mode l, a set of $k = 1, \dots, N$ ridges $a_l^{(k)}(t)$ is obtained, and a procedure to retain only one ridge for the instantaneous frequency must be then made, in [13], for example assuming the average of the k signals:

$$a_l^{\text{mean}}(t) = \frac{1}{N}\sum_{k=1}^{N} a_l^k(t) \tag{25}$$

An alternative way of obtaining a single ridge $a_\Sigma^{(l)}(t)$ for mode l instead of several ridges $a_l^{(k)}(t)$ (one for each measurement point) has recently been proposed by the authors in [8]. This new procedure is based on the computation of the Averaged Continuous Wavelet Transform (ACWT) $\widetilde{T_\psi}[\boldsymbol{u}](a,t)$, which combines the CWTs of each measurement point u_k ($k \in [1, N]$), as follows:

$$\widetilde{T_\psi}[\boldsymbol{u}](a,b) = \sum_{k=1}^{N} [T_\psi[u_k](a,b)]^2. \tag{26}$$

Eq. (26) is suitable for ridge extraction in the case of free responses of systems whose Eigenvectors are real or with a negligible imaginary part, which is the case of weakly damped systems [26] which is practically all civil engineering structures. In fact, the use of the squares of the transforms makes it possible to orient the contributions of the useful signal in each measurement channel according to the same orientation in the complex plane, while those of the noise remain a priori randomly distributed. Therefore, Eq. (26) allows to obtain a single ridge $a_\Sigma^{(l)}(t)$ for mode l as follows:

$$a_\Sigma^{(l)}(t) = arg_a max\left|\left[\widetilde{T_\psi}[\boldsymbol{u}](a,t)\right]\right|^{\frac{1}{2}} = arg_a max\left|\sum_{k=1}^{N}\left[T_\psi[u_k](a,t)\right]^2\right|^{\frac{1}{2}}. \tag{27}$$

Finally, for both definitions of the ridges, i.e. $a_l^{\text{mean}}(t)$ (Eq. 24), or $a_\Sigma^{(l)}(t)$ (Eq. 27), a procedure has been proposed in [8] to smooth the result of the maxima obtained for each time t; for two neighbouring points in frequency of a maximum to the right and to the left make it possible to perform a parabolic interpolation from which we obtain the coordinates of a new ridge in the time scale plane for the mode l under consideration $(t, \breve{a}_k^{(l)}(t))$, or $(t, \breve{a}_\Sigma^{(l)}(t))$. A procedure for chaining the discrete points of the time-frequency plane to transform them into ridges is finally performed (cf. [4]). The set of maxima of the absolute value of the CWT along the ridges present in the signal forms the skeleton of the CWT of the signal. According to the definition chosen for a ridge l in eq. (24) or in eq. (27), the absolute value of the CWT along each ridge $T_\psi[u]\left(\breve{a}_k^{(l)}(t), t\right)$ or the ACWT along the single ridge $\widetilde{T_\psi}[\boldsymbol{u}]\left(\breve{a}_\Sigma^{(l)}(t), t\right)$ is preferred.

4 SYSTEM DYNAMIC CHARACTERIZATION

The modal parameters of a system under transient vibrations can be identified by extracting the ridges and the skeleton of the CWT time-frequency representation. Once the ridges of the CWT have been extracted, the instantaneous frequencies, modal damping ratio and modal shapes can be estimated. If the system is purely linear, the shape of the ridges associated with the Eigenfrequencies will be a straight horizontal line. Furthermore, the damping ratio of the modes of interest can be estimated from the exponential decrease in amplitude associated with these ridges, and finally the modal shapes can be obtained from the relative amplitudes and phase shifts between the channels corresponding to the different sensors.

Therefore, the extraction of the “ridges” is a critical aspect for the successful application of the CWT for modal identification in the case of transient structural responses. Among the authors who have used the CWT for modal identification from transient structural responses, we can cite two references published in 1997: Staszewski [29] and Ruzzene *et al.* [30]. Staszewski [29] proposed several CWT-based methods for estimating damping ratios and applied them to simulated multi-degree-of-freedom systems. Ruzzene *et al.* [30] showed that the CWT analysis of the free response of a system allows the estimation of its natural frequencies and viscous damping ratios. A more complete procedure, which also gives access to frequencies and modal shapes, can be found in Lardies & Gouttebroze [31]. In Le & Argoul [13], the authors found a more precise and complete method where the choice of the mother wavelet, its quality factor and the management of the edge effects of the TOC are studied in depth. The subsequent article by Erlicher & Argoul [27] discusses the use of this procedure in the case of systems with non-proportional damping, and therefore in the presence of complex deformations.

For amplitude and phase modulated signals of the form: $u(t) = A(t)\cos(\phi(t))$, the restriction of the wavelet transform to its ridge behaves mainly as the associated complex signal of $u(t) : A(t)\exp[i\phi(t)]$. This representation also allows the reconstruction of such original signals in non-significant noise situations [4]. If the system behaviour is close to be linear, from the CWT (or the ACWT) of its transient responses, the extracted ridges are similar to horizontal lines and the associated skeleton has an exponential decrease [13]. The logarithm $\log\left|\widetilde{T_\psi}[\boldsymbol{u}](\breve{a}_k^{(l)}(t),t)\right|$ for the CWT, or $\log\left|\widetilde{T_\psi}[\boldsymbol{u}](\breve{a}_\Sigma^{(l)}(t),t)\right|$ for the ACWT can be then deduced and the calculation of the slope of the "straight lines" for each mode l can be performed in order to estimate the corresponding modal damping ratio of the l-th mode. The slope allows to get an estimate to the near sign of the product $2\pi\, f_l\, \xi_l$ that is the reciprocal of the time constant characterizing the exponential decay of the l-th mode.

The calculation of the Eigenshapes requires a set of measurements grouped in the vector: $\mathbf{u} = [u_1, u_2, \cdots, u_N]^T$. The CWT of each component of $\mathbf{u}$ along the smoothed ridge $\breve{a}_\Sigma^{(l)}$ of mode l are also grouped in the vector $\boldsymbol{T_\psi}[\mathbf{u}]$, as follows:

$$\boldsymbol{T_\psi}[\mathbf{u}](\breve{a}_\Sigma^{(l)}(t),t) = \left[T_\psi[u_1](\breve{a}_\Sigma^{(l)}(t),t), T_\psi[u_2](\breve{a}_\Sigma^{(l)}(t),t), \cdots, T_\psi[u_N](\breve{a}_\Sigma^{(l)}(t),t)\right]^T \quad (28)$$

Depending on the choice made for the definition of the ridge, i.e. either Eq. 24, or Eq. 27, the instantaneous complex modal shapes $\phi^{(l)}(t)$ can be derived from the relative amplitude and phase of the CWT calculated along each ridge. There are several ways to normalise the modal vector. One way is to choose the unit amplitude for the measurement point $u_{\max}$, where the $\max$ index corresponds to the measurement point where the modal amplitude is greatest [13]. The k-th component $\phi_k^{(l)}(t)$ of the "instantaneous" complex mode can be expressed as follows:

$$\phi_k^{(l)}(t) = \frac{T_\psi[u_k](\breve{a}_k^{(l)}(t),t)}{T_\psi[u_{max}](\breve{a}_l^{(l)}(t),t)}. \quad (29)$$

In this paper, we prefer the following scaling condition: $(\phi^{(l)}(t))^{\mathrm{T}}\,\phi^{(l)}(t) = 1$ for instantaneous mode shape $\phi^{(l)}(t)$ [8, 10]. This definition results to:

$$\phi_k^{(l)}(t) = \pm\frac{\mathrm{T}_\psi[u_k](\breve{a}_\Sigma^{(l)}(t),t)}{\left[\mathrm{T}_\psi[\mathbf{u}](\breve{a}_\Sigma^{(l)}(t),t))^{\mathrm{T}}\,\mathrm{T}_\psi[\mathbf{u}](\breve{a}_\Sigma^{(l)}(t),t))\right]^{1/2}}, \quad (30)$$

where the sign follows the continuity of $\phi_k^{(l)}$ over time. The amplitude of mode l is then equal to:

$$A_l(t) = \left|\mathrm{T}_\psi[\mathbf{u}](\breve{a}_\Sigma^{(l)}(t),t)^{\mathrm{T}}\,\mathrm{T}_\psi[\mathbf{u}](\breve{a}_\Sigma^{(l)}(t),t)\right|^{1/2} \quad (31)$$

To obtain a "constant" mode, especially in the case of linear behaviour, the mean value over time, denoted $\overline{\phi}$, can be calculated for each component k of the l-th mode:

$$\overline{\phi_k}^{(l)} = \frac{1}{t_f - t_i} \int_{t_i}^{t_f} \phi_k^{(l)}(t)\, dt. \tag{32}$$

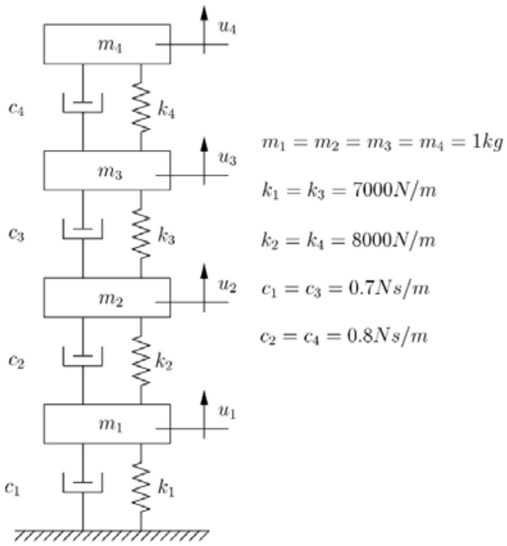

Figure 6: Properties of the four degree-of-freedom system [13].

5 NUMERICAL EXAMPLES

5.1 Transient response of a four degree-of-freedom structure

The first example is the mass spring–damper model with four degrees of freedom. This example was initially studied by Le and Argoul [13] and is here revisited. The properties of the system are shown in Figure 6. The structure is displaced from original position by imposing initial displacements: $u_1 = 1.00$m, $u_2 = 0.75$m, $u_3 = 0.50$m and $u_4 = 0.25$m and zero velocities ($\ddot{u}_1 = \ddot{u}_2 = \ddot{u}_3 = \ddot{u}_4 = 0$). The system is left to freely oscillate after the initial displacements. The sample of duration $L = 5$ sec is taken over $M = 1024$ points (sampling period $T = 0.0049$ sec). The wavelet analysis is performed using the Cauchy wavelet, while for the edge effect we assume $c_t = c_f = 3$.

Figure 7 shows the displacement response histories of the four degrees-of-freedom, while Figure 8 shows the Fourier transform plot for u_1. The four modes can be clearly identified. Furthermore, Figure 9 shows the modulus of the squared averaged CWT (ACWT) transform for three Q_m values, i.e $Q_m = 5, 15$ and 30. The large Q_m value ($Q_m = 30$) allows to clearly see the Eigenfrequencies, but the edge effects become more prominent, since the Q_m value assumed the maximum value $Q_m^{(max)}$ according to Eq. 15 (see also Table 2).

Figure 10a shows the squared averaged CWT (ACWT) for $Q_m = 20$ and the four ridges identified, i.e. $a_\Sigma^{(i)}(t)$, $i = 1, 2, 3, 4$. Due to the linear response, the ridges are straight, while notice that due to the large Q_m value, the ridge identification of the first mode is restricted by the edge effects. Moreover, 10b shows the plots of $\widetilde{T}[\boldsymbol{u}](a, b)$ of the squared averaged CWT transform ridges versus time and the corresponding ridges $\alpha_\Sigma^{(l)}(t)$. The slope of each curve provides the modal damping ratio. Notice that, since the ACWT is squared (see Eq. 26), the slope should be divided by 2. Finally, Figure 11 shows the four averaged Eigenmodes $\overline{\phi}$ obtained after applying Eq. 30 and Eq. 32. The integration limits $[t_f, t_i]$ of Eq. 32 are determined by the edge effects for the frequency of interest.

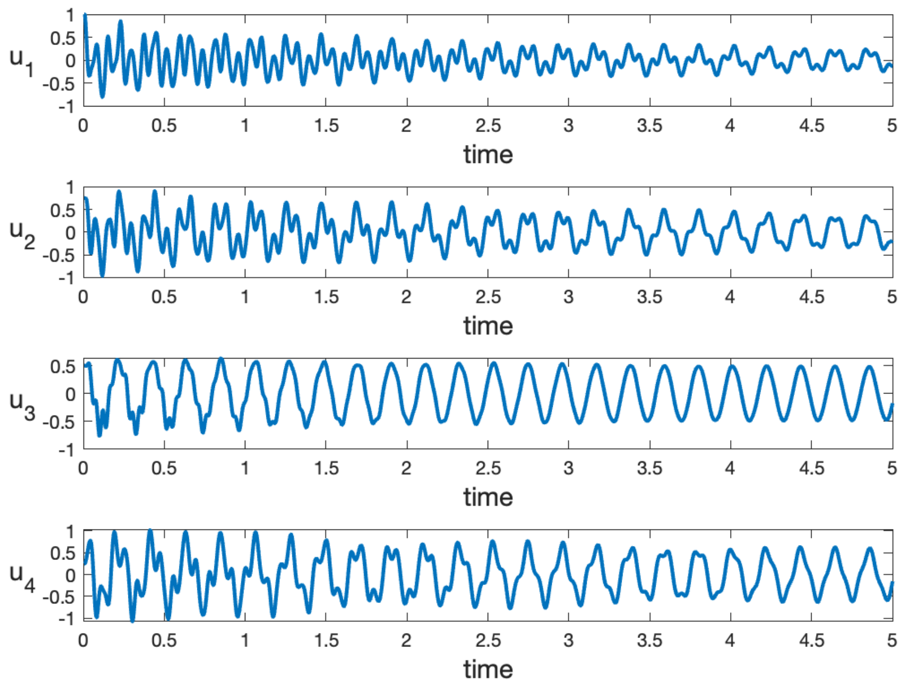

Figure 7: Response histories for the four degree-of-freedom system.

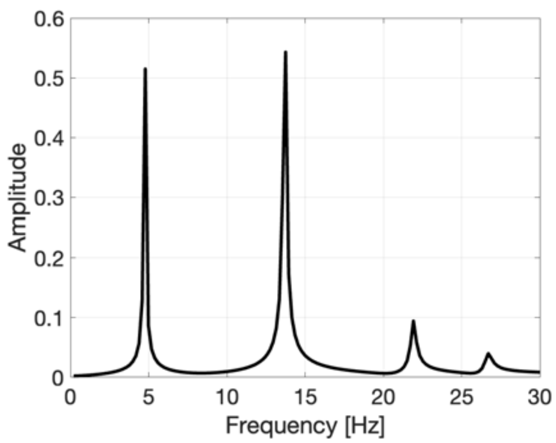

Figure 8: Fourier amplitude spectrum of u_1 response history.

Table 2 summarizes the results of this first example. The first three columns provide the minimum and maximum values of the Q_m parameter obtained with Eq. 15. Since the problem is simulated, the exact Eigenfrequencies and the modal damping ratio values have been exactly

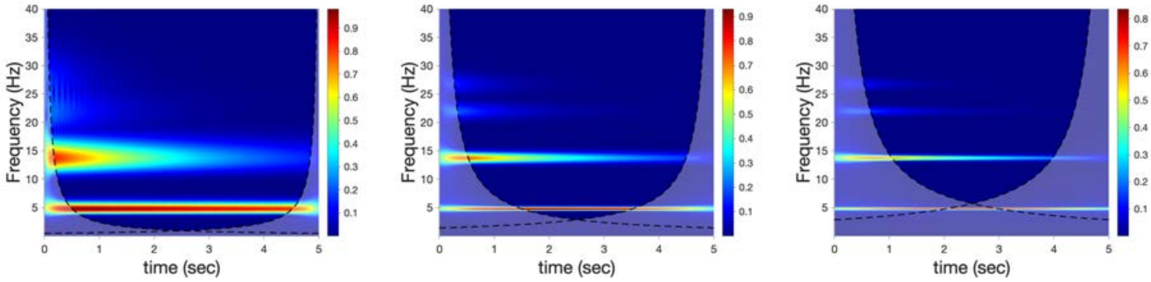

(a) (b) (c)

Figure 9: Scalogram $\widetilde{T_\psi}[\boldsymbol{u}](a,b)$ computed for: (a) $Q_m = 5$, (b) $Q_m = 15$, (c) $Q_m = 30$.

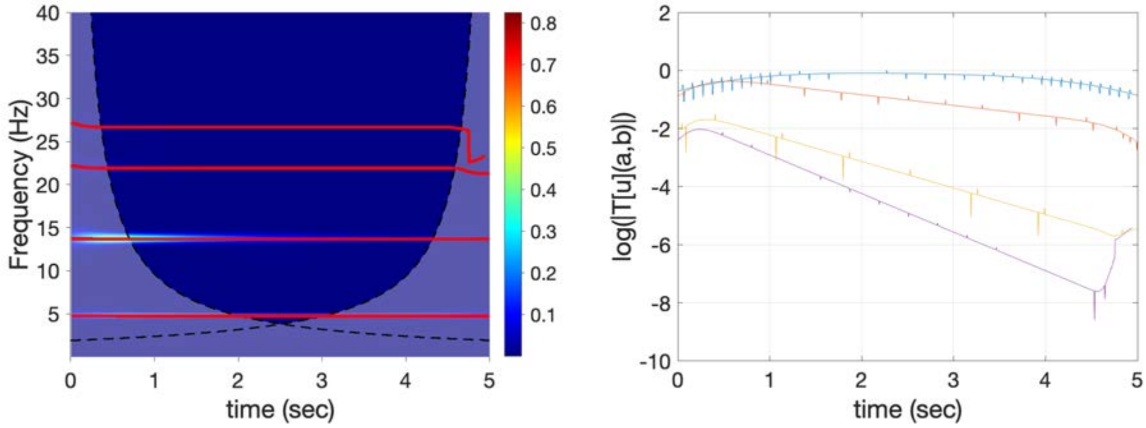

(a) (b)

Figure 10: (a) Scalogram $\widetilde{T_\psi}[\boldsymbol{u}](a,b)$ (computed with: $Q_m = 20$) and ridges identified, (b) damping calculation from the slope of log of the ridge. Note that since the ACWT transform is the sum of transforms that are in the power of two (Eq. 26), the slope of $\log\left(\left|\widetilde{T_\psi}[\boldsymbol{u}](a,b)\right|\right)$ has to be divided by 2.

calculated. Table 2 compares the exact values with those obtained with the aid of the proposed CWT approach, proving its accuracy and efficiency.

5.2 Non linear Single Degree-of-Freedom oscillator subjected to transient loading

The second example is a non linear Single-Degree-of-Freedom (SDoF) oscillator subjected to a sinusoidal harmonic force that stops abruptly after four and a quarter load cycles. When the force is stopped, the system is left to oscillate freely. The applied force is shown graphically in Figure 12a. The maximum value of the force is F_{max} and the instant at which it suddenly stops is shown with a red dashed line. The time instant t_0 is equal to $4.25T_h$, where T_h is the period of the harmonic force. The force-displacement capacity curve of the SDoF oscillator is elastic-perfectly plastic and u_y and F_y are the yield force and yield displacement of the SDoF oscillator, respectively. When the maximum force F_{max} exceeds F_y, the response is inelastic and when $F_{max} < F_y$ the system behaves elastically. In this work it is assumed that the yield force is equal to 50% of the building weight, thus: $F_y = 0.5W$. The yield displacement is obtained as: $d_y = F_y \,/\, k$. If the stiffness of the structure is function of its Eigenfrequency f_s, i.e

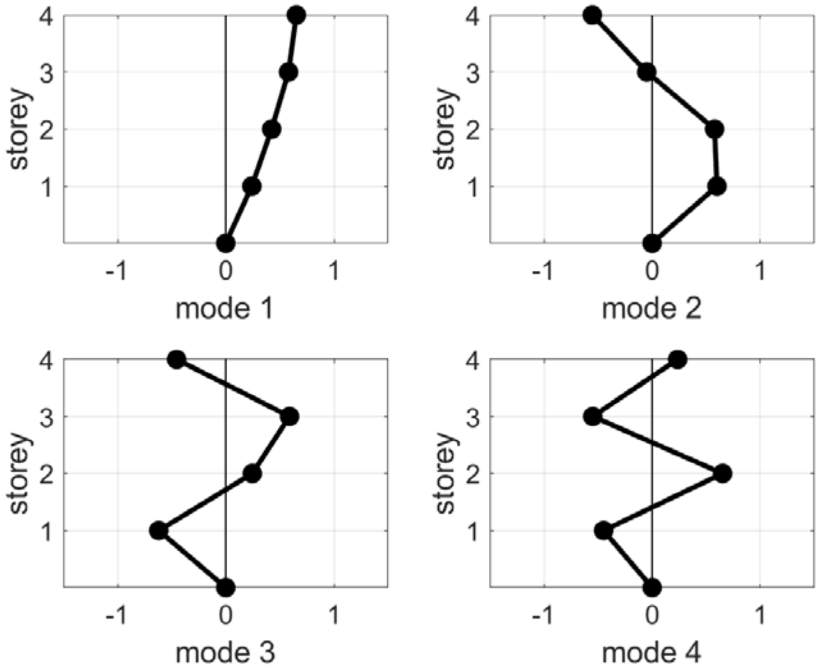

Figure 11: The four Eigenmodes obtained using Eq. 30.

Table 2: Modal properties identified using the CWT method.

Mode	Q_m			Eigenfrequency f (Hz)		Damping ratio ξ	
	Δf (Hz)	min	max	exact	identified	exact	identified
1	4.7397	1.50	24.9	4.7397	4.7430	0.015	0.0017
2	8.8503	2.3	71.4	13.5900	13.6915	0.0043	0.0042
3	7.9135	4.08	112.9	21.5035	21.9165	0.0068	0.0066
4	4.4379	8.8	136.3	25.9414	26.6851	0.0081	0.0079

$k = 4\pi^2 m f_s$, then some after manipulations it is found that: $d_y = F_y / (4\pi^2 m f_s) = 5 / (4\pi^2 f_s)$.

For the example considered, the oscillator has Eigenfrequency equal to $f_s = 0.5$Hz, damping 2% and is subjected to a harmonic force with frequency $f_h = 0.2$Hz and amplitude $2W$, where $W = mg$ is the total weight of the structure. Therefore, the applied force is given by the expression: $F(t) = 2W \sin(2\pi f_h t)$ and $F_{max} = 2W$.

Figure 13 shows the acceleration and the displacement response histories of the elastic perfectly plastic oscillator. The hysteretic model adopted is a bilinear model and the corresponding hysteretic loop is shown in Figure 12b. More details about the hysteretic model can be found in reference [32]. The response accelerations of the elastic and the corresponding inelastic system are shown in Figure 13a. The gray line reaches a maximum acceleration equal to 10g, thus it is that of the elastic case, while the black curve is the inelastic response. A vertical dashed red line marks the time $t_0 = 4.25T_h = 21.25$sec where the force is abruptly stopped. It is can be seen that, for the elastic SDoF, the sudden stop of the force results to an impact that amplifies the response acceleration, this amplification is not visible in the displacement plot on the right.

Figure 14 shows the time-frequency plots of the acceleration signals of Figure 13. The

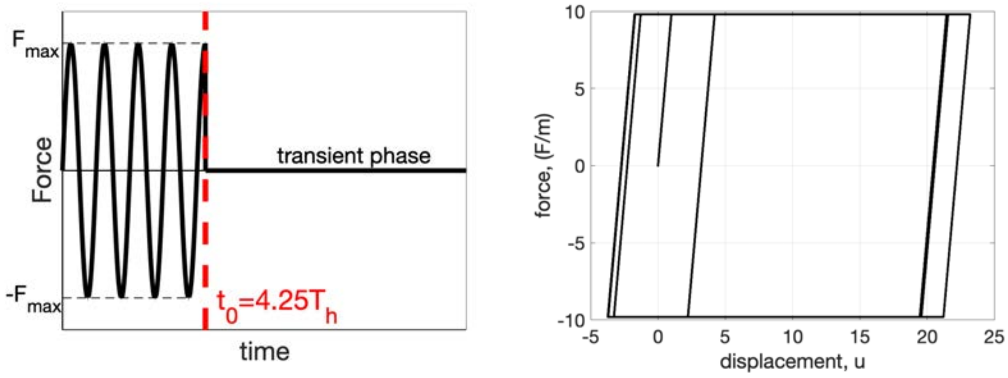

(a) (b)

Figure 12: (a) Applied force $F(t)$, (b) force-displacement curve of the SDoF oscillator considered.

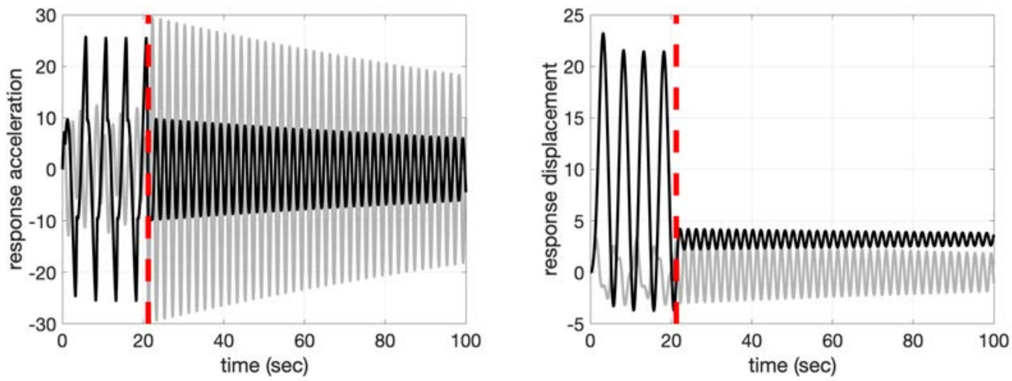

(a) (b)

Figure 13: Elastic and the elastoplastic SDoF oscillator: (a) acceleration response history, (b) displacement response history (black: inelastic response, gray: elastic)

.

resolution parameter value adopted is equal to $Q_m = 8$, while the maximum value using Eq. 15 is equal to $Q_m^{(max)} = 104.72$ and the low bound is $Q_m^{(min)} = 1.5$. The plot on the left shows the response of the elastic case, while the inelastic behaviour is shown on the right. As before, in both plots, the vertical dashed line corresponds to the time instant that the force is stopped. Focusing on Figure 13a, left of the red line, two characteristic frequencies can be identified: that of the Eigenfrequency of the structure at $f_s = 0.5$Hz and that of the harmonic force at $f_h = 0.2$Hz. When the structure enters the free response phase, the amplitude of the modulus of the CWT transform is almost double than that of the harmonic force phase, allowing the ridge and the dominant frequency to be clearly identified. The closed-form solution of the first phase (response under the harmonic force) can be found in various textbooks, e.g. [33]. The response has a transient and a steady component, where the transient component depends on the initial conditions and dies out quickly. Similar findings can be obtained from the plot of the modulus of the CWT of the displacement signal, shown in Figure 15.

Figure 14b shows the scalogram of the inelastic signal plotted in Figure 13b. The CWT method again identifies the Eigenfrequencies of the structure and of the harmonic load. In this case, unlike the elastic case (Figure 13a), the maximum amplitude (skeleton) of the CWT after load removal is reduced compared to that of the CWT during load application. In addition, during the harmonic loading phase ($t < t_0$), we observe energy dissipation at higher frequencies in Figure 14. These ridges appear at frequencies that are odd multiples of the excitation frequency $f_0 = 0.2$Hz : $(2p + 1)\, f_0$, where the cases $p = 1, 2, 3, 4$ are visible in the figure 14b and correspond to superharmonics of the periodic response of the system to harmonic excitation. This is in contrast to the linear case where the response to a harmonic force is harmonic at the same excitation frequency, as shown in the Figure 14a.

The scalogram of the displacement signal is shown in Fig. 15. Most of the observation of Figure 14 can be verified, especially for the elastic case. In the case of inelastic response (Fig. 15b), the superharmonics are not visible. Such information is easier to extract from accelerations which tend to amplify the high frequencies as opposed to the displacement signals. Moreover, the free response amplitude of the CWT modulus is considerably smaller compared to that the harmonic part. This is in agreement with the response histories of Fig.13b), since due to the normalization chosen the module of the CWT provides the amplitude of the signal.

Figure 17, repeats the CWT calculations of Figure 14a and b, increasing the resolution of the time axis by reducing the resolution parameter Q_m to 2. Furthermore, the time scale is restricted to the harmonic phase of the response. "Time discontinuities" at higher frequencies can be clearly seen in both plots. A time discontinuity induces a vertical line in the time-frequency plane corresponding to sudden changes either in the load or at the stiffness of the system. Some researchers call them "spikes", as in [34, 35], who used the Discrete Wavelet Transform method to identify them. Note that the spike due to the sudden change the the load at t_0 is stronger and appears at both scalograms of Figure 17. On the other hand, discontinuities/spikes due to the change of the stiffness, appear only in the inelastic case (Fig. 17b), are milder and take place at increments of $0.5T_h$, i.e. at every peak of the applied load (Fig. 12a).

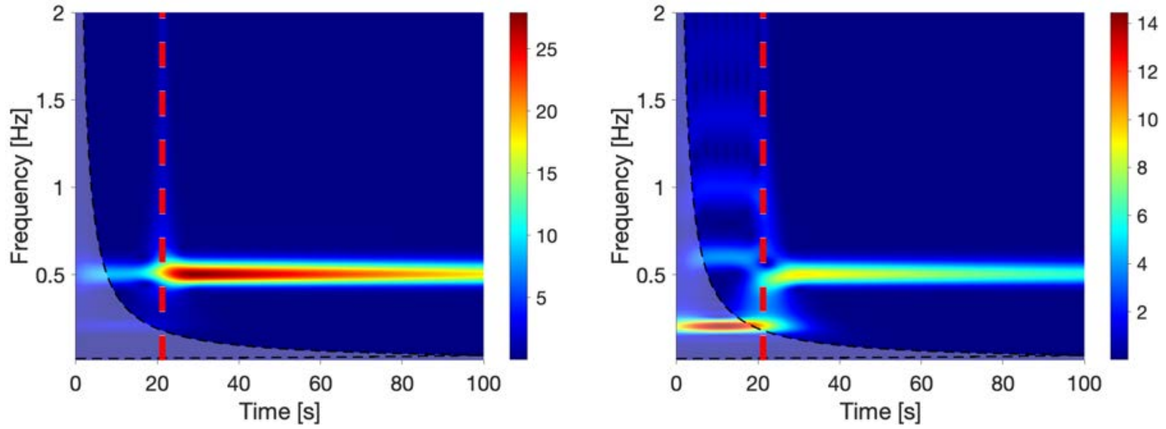

(a)

(b)

Figure 14: Scalogram of the acceleration signal shown in Figure 13a $\left|T_\psi[\ddot{u}](a, b)\right|$: (a) elastic behaviour, (b) inelastic behaviour ($Q_m = 8$).

6 CONCLUSIONS

The wavelet analysis method allows the representation of the processed signal in the time-frequency plane, thus facilitating access to the estimation of the modal characteristics or of the

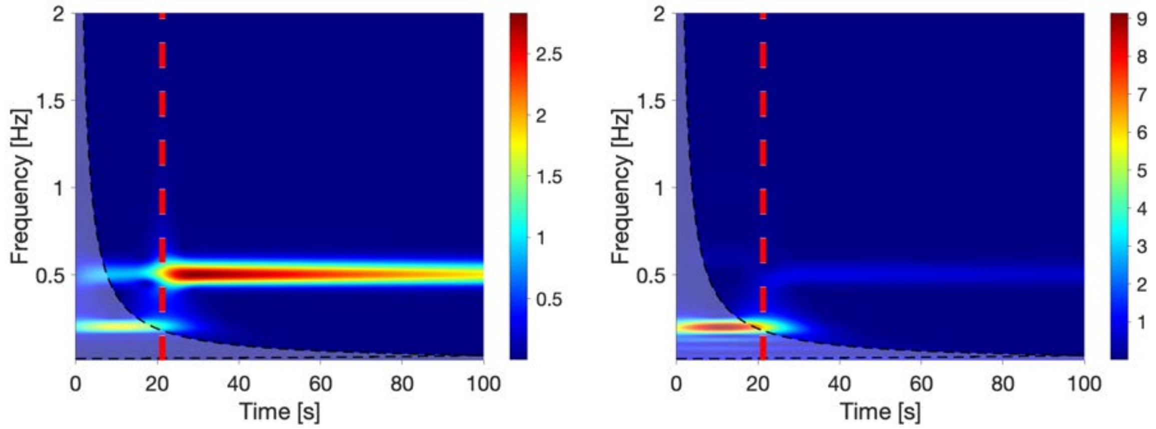

(a) (b)

Figure 15: Scalogram of the displacement signal shown in Figure 13b $\left|T_\psi[u](a,b)\right|$: (a) elastic behaviour, (b) inelastic behaviour ($Q_m = 8$).

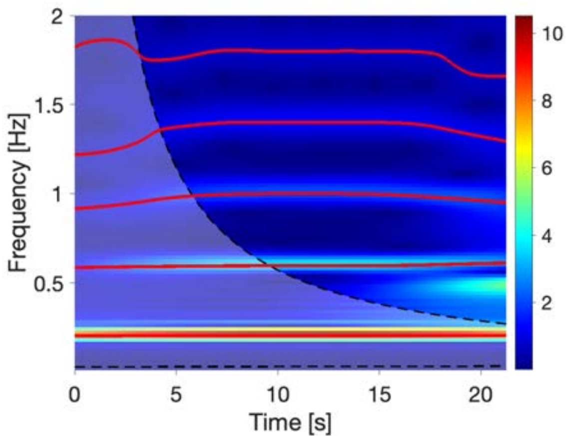

Figure 16: Focus of Figure 14b in order to present the ridges at which the system vibrates when the response is nonlinear. Notice that the super-harmonics in pink appear at frequencies at $(2p + 1)f_0$, where $f_0 = 0.2$Hz and $p = 1, 2, 3, 4$. ($Q_m = 8$)

structural defects (localisation in time and severity of the damage). Two application examples are presented which show that the CWT method can be used to efficiently handle inverse problems and provide valuable information for structural modal identification and also for damage assessment.

ACKNOWLEDGMENTS

The authors would like to thank his two former doctoral students Nicolas Vacca and Raphaël Carpine for their thesis work [9, 10] respectively, and a student trainee at the Ecole des Ponts ParisTech Mohammed-Ta Hamzaoui for his help in drawing several figures in this article. They are also very grateful to Charles Cynober of Freyssinet for authorising the use of the set of measurements concerning the passage of a semi-trailer over a joint in the pavement of a road bridge. They express their deep appreciation to Françoise Argoul for proofreading this article and for her wise advice and expertise on the use of the wavelet transform. The second author

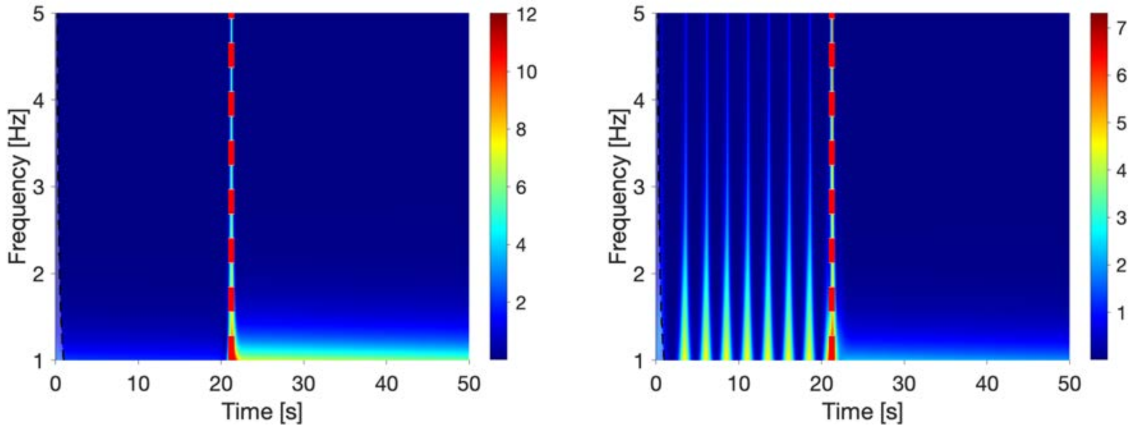

(a) (b)

Figure 17: Focus of the scalogram of the acceleration signal $\left|T_\psi[\ddot{u}](a,b)\right|$ in order to study the observed spikes: (a) elastic behaviour, (b) inelastic behaviour. (Q_m = 2)

would also like to thank the Université Gustave Eiffel for its financial support through the 'iSite-FUTURE' project.

REFERENCES

[1] Mallat, S. (1989). "A theory of multiresolution signal decomposition: The wavelet representation." *IEEE Transactions on Pattern Analysis and Machine Intelligence*, 11:674-693.

[2] Grossmann, A. and Morlet, J. (1984). "Decomposition of Hardy functions into square integrable wavelets of constant shape." *SIAM Journal on Mathematical Analysis*, 15(4):723-736.

[3] Mallat S.G. (1989). "Multiresolution approximations and wavelet orthonormal bases of L2(R)" *Trans. Amer. Math. Soc*, 315, 69-87.

[4] Carmona, R., Hwang, W-L. and Torrésani, B. "Practical Time-Frequency Analysis: Gabor and wavelet transforms, with an implementation in S", *Wavelet Analysis and its Applications, Vol. 9*, Academic Press, San Diego, 1998.

[5] Chassande-Mottin E., Flandrin P. (1998) "On the stationary phase approximation of chirp spectra." *Proc. IEEE Int. Symp. on Time-Frequency and Time-Scale Analysis*, Pittsburgh, 117–120.

[6] Flandrin, P. (1999). "Time-Frequency/Time-Scale Analysis" *Wavelet Analysis and its Applications*, Vol. 10) Academic Press, San Diego.

[7] Chatterjee P. (2018). "Wavelet Analysis in Civil Engineering" *CRC Press*, isbn = 978-1-4822-1056-9.

[8] Carpine R., Ientile S., Vacca N., Boscato G., Rospars C., Cecchi A., Argoul P. (2021). "Modal identification in the case of complex modes – Use of the wavelet analysis applied to the after-shock responses of a masonry wall during shear compression tests.", *Mechanical Systems and Signal Processing*, 160, 107753.

[9] Vacca, N. (2022). “Fonctions analytiques et signaux asymptotiques pour la transformée en ondelettes” (’Analytic functions and asymptotic signals for the wavelet transform’), *PhD thesis of Paris-Est University*, 29-04-2022, in French.

[10] Carpine R. (2022). “Détection de défauts dans les structures de génie civil par analyse en ondelettes de réponse vibratoire.”, *PhD thesis of Paris-Est University*, in French.

[11] Argoul, P., Le, T.P. (2004). “Wavelet Analysis of Transient Signals in Civil Engineering”. In: Frémond, M., Maceri, F. (eds) Novel Approaches in Civil Engineering. *Lecture Notes in Applied and Computational Mechanics*, Vol 14. Springer, Berlin, Heidelberg.

[12] Argoul, P., Le, T.-P. (2003). “Instantaneous indicators of indicators of structural behaviour based on the continuous Cauchy wavelet analysis”, *Mechanical Systems and Signal Processing*, 17(1), 243-250.

[13] Le T.-P., Argoul, P. (2004). “Continuous wavelet transform for modal identification using free decay response”, *Journal of Sound and Vibration*, 277(1-2), 73–100.

[14] Guillet, A., Arneodo, A., Argoul, P. and Argoul, F. (2023). “Quantifying the rationality of rhythmic signals”, In Theoretical Physics, Wavelets, Analysis, Genomics, Springer International Publishing, Series Title: Applied and Numerical Harmonic Analysis, Flandrin, P., Jaffard, S. , Paul, T. and Torresani, B. Editors, 565–593.

[15] Lilly, J.M. (2017). “Element analysis: A wavelet-based method for analysing time-localized events in noisy time series”, *Proceedings of the Royal Society A: Mathematical, Physical and Engineering Sciences*, 473(2200).

[16] Olhede S. C. & Walden A. T. (2002). “Generalized Morse wavelets.” *IEEE Transactions on Signal Processing*, 50(11), 2661-2670.

[17] Lilly J. M. & Olhede S. C., (2009). “Higher-Order Properties of Analytic Wavelets.” *IEEE Transactions on Signal Processing*, 57(1), 146-160.

[18] Daubechies I. & Paul T. (1988). “Time-frequency localization operators—A geometric phase space approach: II. The use of dilations,” *Inverse Problems*, Vol. 4, pp. 661–680.

[19] Lilly J. M. & Olhede, S. C. (2012). “Generalized Morse Wavelets as a Superfamily of Analytic Wavelets” in *IEEE Transactions on Signal Processing*, Vol. 60(11): 6036-6041.

[20] Mallat, S., Waldspurger, I. (2015). “Phase Retrieval for the Cauchy Wavelet Transform.” *J Fourier Anal. Appl.*, 21:1251–1309.

[21] Rouby C., Rémond, D. and Argoul P. (2010). “Orthogonal polynomials or wavelet analysis for mechanical system direct identification”. *Ann. Solid Struct. Mech.*, 1:41–58.

[22] Delprat, N., Escudie, B., Guillemain, P., Kronland-Martinet, R., Tchamitchian, P., & Torresani, B. (1992). “Asymptotic wavelet and Gabor analysis: extraction of instantaneous frequencies.” *IEEE Transactions on Information Theory*, 38(2): 644–664.

[23] Torrésani, B. (2012). “Analyse continue par ondelettes.”, EDP Sciences, 256 pages.

[24] Lilly, J. M., & Olhede, S. C. (2010). "On the Analytic Wavelet Transform." *IEEE Transactions on Information Theory*, 56(8): 4135–4156.

[25] Carmona, R., Hwang, W. L., & Torrésani, B. (1995). "Identification of chirps with continuous wavelet transform." In P. Bickel, P. Diggle, S. Fienberg, K. Krickeberg, I. Olkin, N. Wermuth, S. Zeger, A. Antoniadis, & G. Oppenheim (Eds.), *Wavelets and Statistics*, 103:95–108. New York.

[26] Geradin M. & Rixen D.-J. (2015). "Mechanical Vibrations: Theory and Application to Structural Dynamics", John Wiley & Sons, 616 pages.

[27] Erlicher, S., Argoul, P. (2007). "Modal identification of linear non-proportionally damped systems by wavelet transform." *Mechanical Systems and Signal Processing*, 21(3): 1386–1421.

[28] Argoul P. and Erlicher S. (2005). "Mechanical modelling and computational issues in civil engineering", Volume 23 of Lecture Notes in Applied and Computational Mechanics, In "On the use of continuous wavelet analysis for modal identification",359-–368. Springer.

[29] Staszewski W.J. (1997). "Identification of damping in MDOF systems using time-scale decomposition", *Journal of Sound and Vibration,* 203(2): 283-305.

[30] Ruzzene M., Fasana A., Garibaldi L., & Piombo B., (1997). "Natural frequencies and dampings identification using wavelet transform: application to real data", *Mechanical Systems and Signal Processing*, 11(2): 207-218,

[31] Lardies, J., Gouttebroze, S. (2002). "Identification of modal parameters using the wavelet transform." *International Journal of Mechanical Sciences*. 44(11): 2263—2283.

[32] Fragiadakis, M (2006). "Nonlinear optimum seismic design of structures". *PhD Thesis*, National Technical University of Athens, April 2006.

[33] Kramer, S. (1996). Geotechnical Earthquake Engineering, Willey.

[34] Hou, Z., Noori, M., Amand, R.St (2000). "Wavelet-Based Approach for Structural Damage Detection." *Journal of Engineering Mechanics*, 126(7), 677–83.

[35] Todorovska, M. I., Meidani, H., Trifunac, M. D. (2009). Wavelet approximation of earthquake strong ground motion-goodness of fit for a database in terms of predicting nonlinear structural response. *Soil Dynamics and Earthquake Engineering*, Vol. 29(4): 742—751.